Optica Applicata, Vol. LIII, No. 2, 2023
DOI: 10.37190/oa230204

Research on characteristics of embedded resonator sensor based on PtS_2

XIN LI, XIEYUAN LI*, HAITAO ZHANG, SHUANG CHEN, SHURONG LIU, YANG LI

School of Mathematics and Information Technology, Hebei Normal University of Science & Technology, Qinhuangdao, 066004, China

*Corresponding author: hey2380@163.com

An embedded microring resonator model using PtS_2 as the core layer was designed and optimized for sensing. The inner layer is made of PtS_2, and SiO_2 and Si_3N_4 are used as cladding. The overall structure is Si_3N_4-SiO_2-PtS_2-SiO_2-Si_3N_4. Field strength distribution of longitudinal section of single straight waveguide and the longitudinal section of coupling part of straight and annular waveguides are simulated according to the coupled-mode theory. The transfer matrix method is used to analyze characteristics between the length of the U-shaped feedback waveguide and the circumference of microring and the change of attenuation factor and coupling coefficient on the output spectrum. The simulation results showed that the embedded microring resonator with PtS_2 as the core presents excellent optical properties. The resonance depth is more than –50 dB, and the sensitivity can reach 1806.61 dB/RIU. When the resonance wavelength is 1550.86 nm and the self -coupling coefficient is 0.9849. The corresponding detection limit is about 1.66056×10^{-7} dB/RIU, and the quality factor is 2.8848×10^{-5} under the measurement system with a signal-to-noise ratio of 30 dB. Compared with the traditional single microring structure, the proposed microring presents a higher free spectral range and more suitable for the fabrication of high-sensitivity, low-detection limit, and large-measurement range sensors.

Keywords: embedded, microring resonator, U-shaped feedback waveguide, PtS_2 core layer.

1. Introduction

Noble transition metal dichalcogenides (TMDCs) are new 2D layered materials after graphene which have recently attracted considerable research attention in the development of optoelectronics. TMDCs are composed of two chalcogenide atoms sandwiched outside the transition metal atoms, with the band gap widening with the decrease of material thickness. TMDCs are widely used in photoelectric detectors, lasers, label-free sensors, and other fields because of their unique optical and electronic properties, such as high carrier mobility [1], high refractive index [2], and tunable band gap [3]. These characteristics are widely used in photoelectric detectors [4,5], lasers [6], label-free sensors [7] and other fields. PtS_2 is a typical representative of two-dimensional transition metal chalcogenides that demonstrates a narrow band gap, requires minimal energy for electron transition and exhibits high refractive index and excellent switching ratio at room temperature. Compared with graphene with zero band gap, PtS_2 with band gap is an ideal material for nanophotonic applications because it shows excellent electrical conductivity and high air stability. Moreover, PtS_2 demonstrates excellent application prospects in photoelectric sensors, photoelectric modulators and other fields [8,9].

Microring resonators are widely used in filtering [10], sensing [11], optical switch [12], optical modulator [13] and other fields due to their advantages of high-quality factors, compact structure and high integration. Many microring resonators have been designed with various structures and materials. Typical structures include series, parallel, and runway. The embedded microring structure coupled with single microring and U-shaped waveguide has been continuously optimized in recent years because it shows satisfactory filtering characteristics, such as high Q factor and extinction ratio. However, its application in the sensing field is rare [14,15]. Reference [16] proved that the sensitivity of the embedded microring structure filter can reach 0.22 dB/mW using experiments. Graphene, diamond, silicon nitride and other materials have been applied to the design of microring resonators. However, studies on the application of PtS_2 materials with high refractive index characteristics to microring resonators are limited. If the embedded microring resonator structure is combined with TMDCs materials with excellent performance, then the structure's performance will be further improved.

We present a single-ring embedded microring resonator based on the Si_3N_4-SiO_2 -PtS_2-SiO_2-Si_3N_4 waveguide structure in this paper. The high refractive index PtS_2 is utilized as the core layer to form a considerable refractive index difference with the cladding, reduce transmission loss, gather light in the core layer, and improve device performance. COMSOL Multiphysics is used to explore the electromagnetic field distribution of longitudinal and transverse sections of the structure under resonant and nonresonant conditions as well as symmetric and asymmetric modes. Transmission matrix theory is applied to investigate the influence of the coupling coefficient, transmission coefficient, quality factor and other related parameters on resonant characteristics of the structure under a resonant wavelength of 1.550 μm. The sensitivity and detection limit under optimized parameters are calculated. The results showed that the embedded microring resonant structure with PtS_2 as the core material presents an extensive free spectral range, high-quality factor and high design freedom. Moreover, this structure sensor's sensitivity, detection limit, detection range, and other sensing characteristics are better than those of the traditional single-loop resonator.

2. Model and theoretical analysis

The PtS_2-based structure of the embedded microring resonator composed of a U-shaped feedback waveguide and a ring resonator is shown in Fig. 1. Coupling regions of the ring cavity and the U-shaped waveguide are denoted I and II, respectively; R is the radius of the ring resonator; L_1 is the length of the U-shaped feedback waveguide;

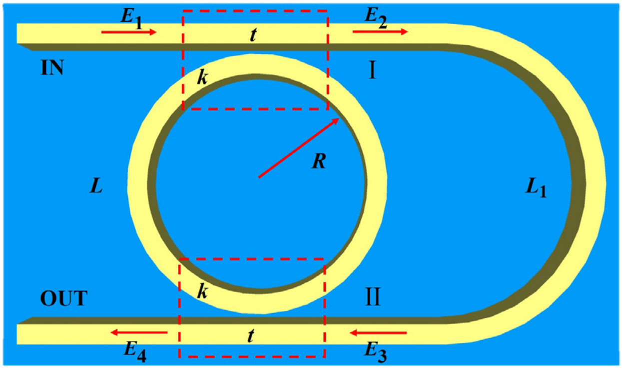

Fig. 1. Embedded microring resonator.

E_1, E_2, E_3 and E_4 are the optical field intensity of each point. We assume that amplitude coupling and self-coupling coefficients of the two coupling parts are k and t, respectively [17], when light field coupling occurs at the tangential point of the ring cavity and the condition $k^2 + t^2 = 1$ is satisfied without coupling loss for the convenience of calculation. According to the coupled-mode theory, the mathematical model of the embedded structure can be established using the transfer matrix method [18].

Figure 1 shows that the transmission matrices of coupling regions I and II are M_1 and M_2, respectively; the transmission matrix between microrings is M_t, and the total matrix of microring transmission is

$$M = M_2 \cdot M_\mathrm{t} \cdot M_1 = \begin{bmatrix} M_{11} & M_{12} \\ M_{21} & M_{22} \end{bmatrix} \tag{1}$$

and

$$M_1 = M_2 = \begin{bmatrix} \dfrac{-t}{ik} & \dfrac{1}{ik} \\ \dfrac{-1}{ik} & \dfrac{t}{ik} \end{bmatrix} \tag{2}$$

$$M_\mathrm{t} = \begin{bmatrix} 0 & p\sqrt{\tau} \\ (p\sqrt{\tau})^{-1} & 0 \end{bmatrix} \tag{3}$$

$$M = \begin{bmatrix} \dfrac{pt\sqrt{\tau}}{k^2} - \dfrac{t}{k^2 p\sqrt{\tau}} & \dfrac{1}{k^2 p\sqrt{\tau}} - \dfrac{pt^2\sqrt{\tau}}{k^2} \\ \dfrac{p\sqrt{\tau}}{k^2} - \dfrac{t^2}{k^2 p\sqrt{\tau}} & \dfrac{t}{k^2 p\sqrt{\tau}} - \dfrac{pt\sqrt{\tau}}{k^2} \end{bmatrix} \tag{4}$$

In Eq. (4), $\tau = \exp(-\alpha L)$ is the transmission coefficient of light in the microring, $L = 2\pi R$, α is the transmission loss coefficient, $p = \exp(i\varphi/2)$ is the phase factor of light transmission in the microring for half a week, $\varphi = \beta L$ is the phase difference generated by the transmission of light signal around the microring for one circle, and $\beta = 2\pi n_{\mathrm{eff}}/\lambda$ is the transmission constant. From the transfer matrix method,

$$\begin{bmatrix} E_3 \\ E_4 \end{bmatrix} = M \begin{bmatrix} E_1 \\ E_2 \end{bmatrix} \tag{5}$$

The relationship between light fields E_3 and E_2 is

$$E_3 = \tau p_1 E_2 \tag{6}$$

The formula of output port light intensity can be derived from the transfer matrix and Eqs. (4) and (5),

$$E_4 = \left(M_{21} - \frac{M_{11} \cdot M_{22}}{M_{12} - \tau_1 p_1} \right) E_1 \tag{7}$$

If a feedback waveguide is absent, then the output light field is

$$E_{\mathrm{out}} = \left(M_{21} - \frac{M_{11} \cdot M_{22}}{M_{12}} \right) E_1 \tag{8}$$

Hence, the output port light intensity can also be expressed as, where E_{f} is an additional light field,

$$E_4 = E_{\mathrm{o}} + \frac{-\tau_1 p_1 M_{11} M_{22}}{M_{12}(M_{12} - \tau_1 p_1)} E_1 = E_{\mathrm{o}} + E_{\mathrm{f}} \tag{9}$$

The normalized function of the output port derived from the transfer matrix is:

$$I = \frac{E_4}{E_1} = \frac{-k^2 \sqrt{\tau}\, p + t^2 \tau_1 p_1 - \tau p^2 \tau_1 p_1}{1 - t^2 \tau p^2 + k^2 \sqrt{\tau}\, p \tau_1 p_1} \tag{10}$$

The output expression of out port can be expressed as:

$$I^2 = \left| \frac{E_4}{E_1} \right|^2 = \left| \frac{-k^2 \sqrt{\tau}\, p + t^2 \tau_1 p_1 - \tau p^2 \tau_1 p_1}{1 - t^2 \tau p^2 + k^2 \sqrt{\tau}\, p \tau_1 p_1} \right|^2 \tag{11}$$

The denominator of the normalized function formula at the output end contains $k^2 \tau^{1/2} p \tau_1 p_1$, which is $k^2 \exp[-\alpha(L/2 + L_1) + i\beta(L/2 + L_1)]$. The output light intensity is significant when L_1 is an integer multiple of $L/2$. This situation is primarily discussed in this study. Essential indicators for measuring the sensing performance are sensitivity, detection limit and Q factor. The sensing sensitivity represents the slope of the spectral line of the output light intensity, that is, the output light intensity variation *versus* the refractive index variation [19]. The sensing sensitivity is expressed as

$$S = \frac{\Delta I_0}{\Delta n} \tag{12}$$

The detection limit represents the minimum information change that the sensor can measure. According to the ratio of the limit of the light intensity measuring instrument to the sensitivity of the sensor, the value of the measurement limit of 0.003 under the signal-to-noise ratio of 30 dB is discussed in this work. The detection limit can be expressed as follows:

$$\delta n = \frac{\delta I}{S} \tag{13}$$

3. Model parameter design

Figure 2 shows the longitudinal section structure of the ridge waveguide. The waveguide width w is 500 nm, waveguide height is 650 nm, and distance s between the two waveguides is 15 nm. The thickness of the outer cladding Si_3N_4 is 400 nm, the middle cladding is silica, and the height is 30 nm; m is the height of the PtS_2 core layer. The thickness of the core PtS_2 is 7 nm, and its refractive index is 3.5 at wavelength of 1.55 μm [20]. The structure is simulated using CMOSOL Multiphysics. The simulation results of the field distribution of the light wave in the longitudinal section of the waveguide are presented in Fig. 3. The high energy region of the electric field is mainly distributed around the core of PtS_2. The weak electric field intensity of the outer layer decreases with the increase of distance from the core. The refractive index difference between outer and central claddings can appropriately gather light in the core. Figures 4(a) and (b) illustrate the field intensity distributions of the longitudinal section of the coupling region between straight and annular waveguides in symmetric and

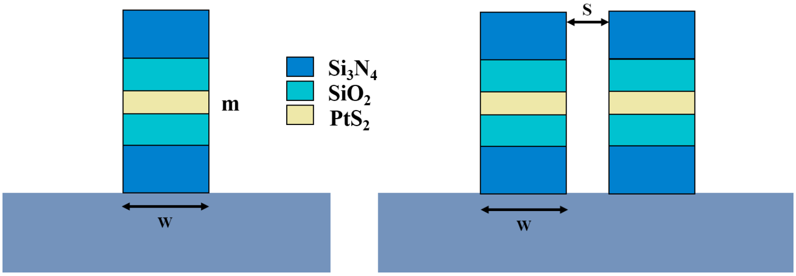

Fig. 2. Schematic diagram of waveguide longitudinal section structure.

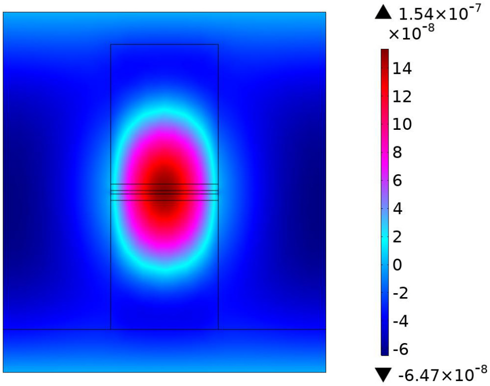

Fig. 3. Field intensity distribution in longitudinal section of a single waveguide.

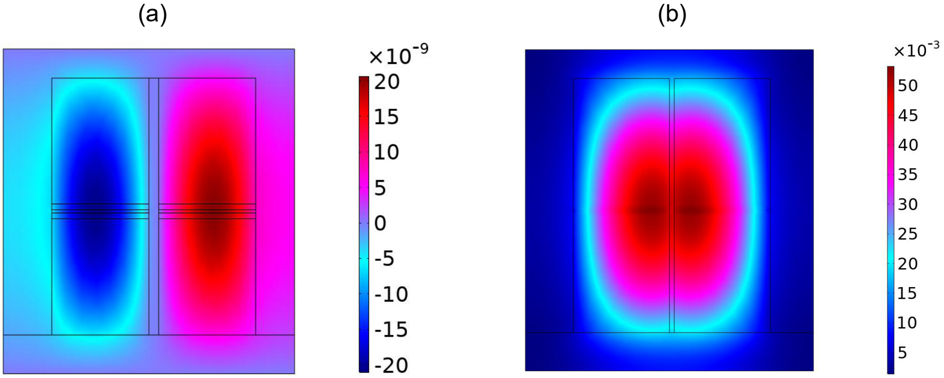

Fig. 4. Field intensity distribution in the longitudinal section of the coupling area between straight and acircular waveguides. (a) Asymmetric mode, and (b) symmetrical mode.

asymmetric modes, respectively. The two modes are essential indicators in the simulation design that affect the length of the coupling region, The light in the upper straight and annular waveguides can be coupled properly when the distance between the two waveguides is 15 nm.

The electric field distribution of the embedded microring resonator when the continuous wave is the input is shown in Fig. 5. Figure 5(a) presents the electric field distribution of the nonresonant state of the embedded microring resonator, where the incident light is not coupled into the ring cavity and transmitted directly to the exit port along the U-shaped feedback waveguide. Figure 5(b) illustrates the electric field distribution of the microring in the resonant state. Most of the light wave enters the ring cavity through the coupling zone I after the light wave is injected into the straight waveguide through the incident port through E_1. The interference-enhanced light wave in the microring is in the resonant state, forms a stable and regular standing wave and is outputted by the E_4 port after recoupling. The diagram demonstrated that the signal is nearly completely concentrated in the annular waveguide at this moment. An inev-

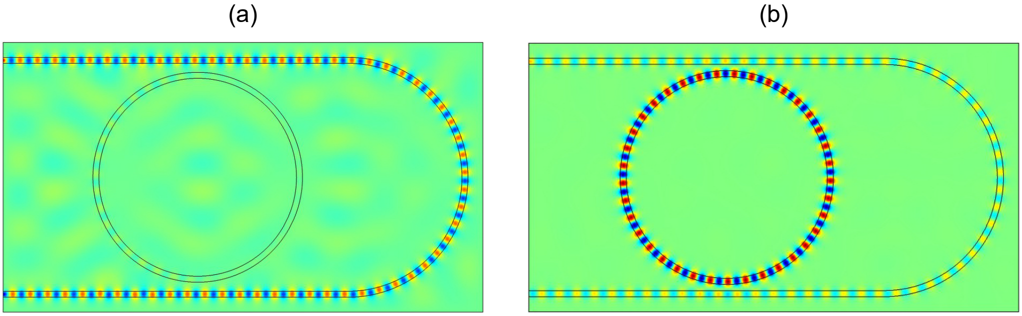

Fig. 5. Electric field distribution of embedded microring resonator. (a) Non-resonant condition, and (b) resonance condition.

itable energy loss occurs in the annular waveguide due to bending. This loss can be compensated by increasing the radius of the microring or changing the material to set a high electric field limit.

Figure 6 depicts the distribution of the electric field in the ring cavity and the U-shaped feedback waveguide of the embedded microring resonator in the form of the electric field height diagram. The transmission light field of the embedded structure consists of two parts: the internal field of the resonator recoupled into the excitation waveguide and U-shaped excitation waveguide. The destructive coherence between the two parts of the light field forms a concave transmission spectrum at the resonance. The light gathers in the annular cavity, and the field height is high. The electric field height in the U-shaped feedback waveguide is low in the microring.

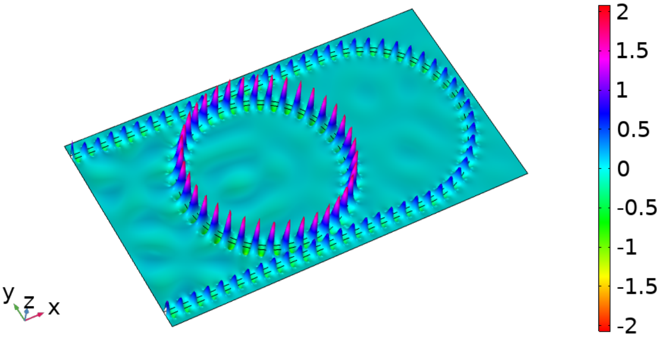

Fig. 6. Electric field height diagram of embedded microring resonator.

Model parameters in this study are designed as follows: working wavelength $\lambda = 1.55086$ μm, $n_{\text{eff}} = 3.5$, $R = 100$ μm, the length of U-shaped waveguide L_1 is equal to the perimeter of the microring, that is, $L_1 = L$. The combined Eq. (11) out port output is simulated using on MATLAB software. The output spectrum of the embedded microring resonant filter, at a wavelength range of 1544–1556 nm is shown in Fig. 7. The output spectrum is periodically distributed, and the top of the passband is flat.

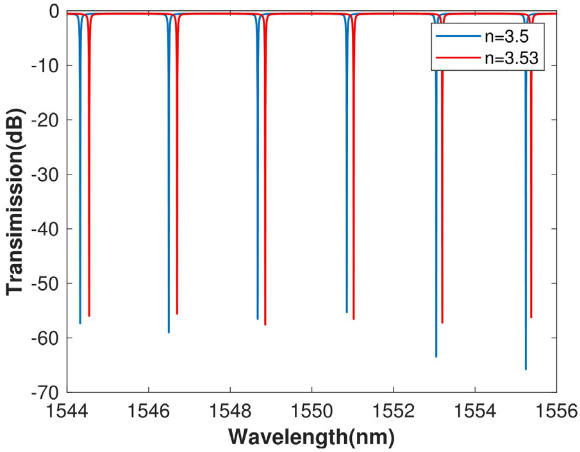

Fig. 7. Output spectra of different refractive indices.

The peak will produce significant displacement, and the intensity can reach a minimum of –50 dB when the refractive index of PtS_2 changes to 0.03. According to the displacement of the resonant wavelength peak, the external environment change can be measured to make different sensors.

4. Analysis of main influence parameters

4.1. Length of U-shape feedback waveguide

The relationship between the length of the U-shaped feedback waveguide and the microring is also an essential factor affecting structural performance. The resonance

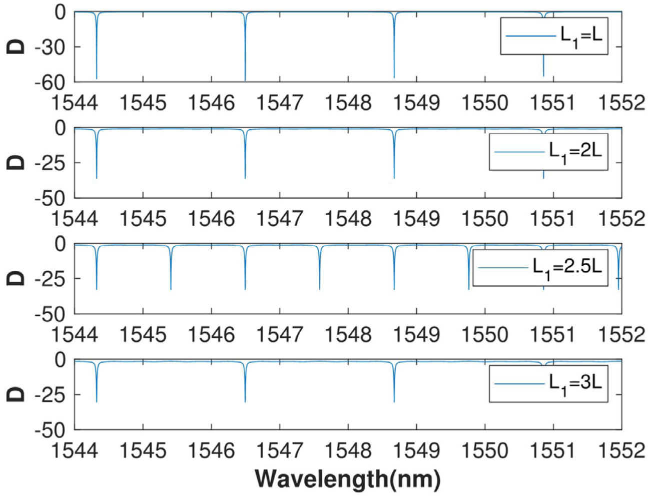

Fig. 8. Output spectra of feedback waveguides with circular waveguides of different ratios.

remains regular when the length of the U-shaped waveguide L_1 is an integer multiple of $L/2$. Here we analyze it in several different multiples. The self-coupling coefficient $t = 0.9849$, the transmission coefficient $\tau_1 = \exp(-\alpha L_1)$, the transmission phase factor $p = \exp(i\varphi)$, the phase change after the transmission of the U-type feedback waveguide $\varphi = \beta L_1$. The spectrum output diagram when the length of the U-type feedback waveguide is different times of the microring perimeter is shown in Fig. 8, respectively, showing the output spectrum when the length of the U-type feedback waveguide is one time, two times, 2.5 times and three times of the ring waveguide length. The FSR changes when the length of the U-type feedback waveguide is different. The resonance peak is prominent and sharp when $L_1 = L$. Hence, this state is chosen for the design with a large FSR and light intensity.

4.2. Self-coupling coefficient *t*

Figure 9 shows that $n = 3.5$ μm and $R = 100$ μm in the wavelength range of 1542 –1556 nm when the feedback waveguide length is the circumference of the ring waveguide and the self-coupling coefficient of the waveguide changes when the normalized output light intensity changes. We assume that t values are 0.2466, 0.6530, 0.9849, and 0.946 respectively for simulation. The analysis of the output light intensity diagram showed that the extinction of the output spectrum is poor when the t value is small. The flatness of the output spectrum reaches the maximum and the output light intensity is the maximum when $t = 0.9849$. Figure 10 presents the accurate analysis of spectrum with self-coupling coefficient approximate range, specifically in the wavelength range of 1550.83–1550.88 nm, near $t = 0.9849$; t takes values 0.9840, 0.9846, 0.9849, 0.9870, 0.9880. The resonant wavelength notch depth increases gradually and the output spectrum becomes sharp and steep when the self-coupling coefficient is 0.9849. The resonance intensity will weaken when other values are taken. The production pro-

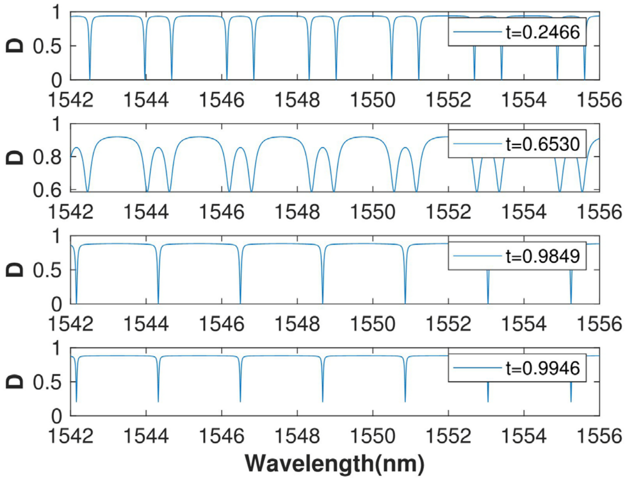

Fig. 9. Output spectral shape with different *t* values.

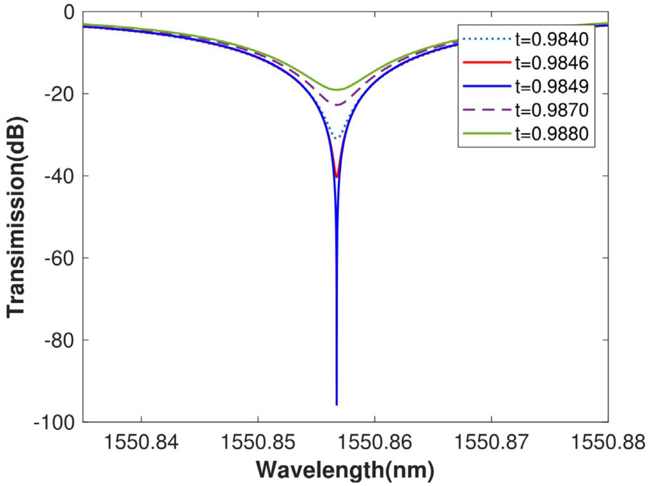

Fig. 10. Accurate analysis of spectrum with self-coupling coefficient.

cess in practical applications should be improved to suppress the loss of the microring resonator as extensively as possible and ensure the transmittance at the central resonance peak.

4.3. Amplitude attenuation coefficient α

Figure 11 illustrates the transmittance characteristics of the passband in the wavelength range of 1550.6–1551.1 nm when different loss values are used in the embedded microring resonator under the ideal coupling condition. The transmission coefficient $\tau = \exp(-\alpha L)$, when the radius of the ring cavity is 100 μm and the value of different

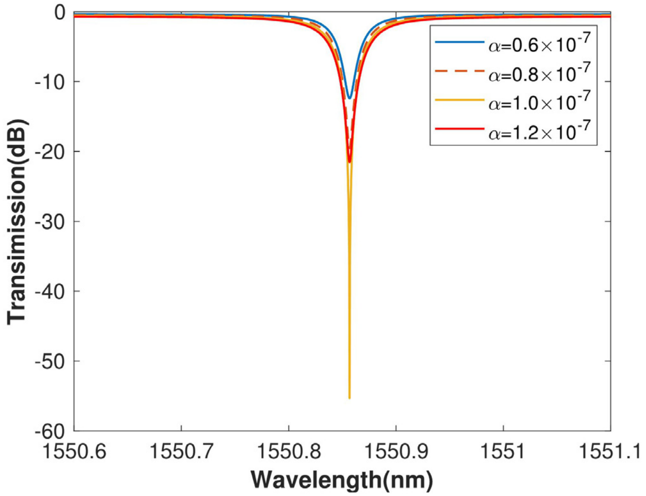

Fig. 11. Output spectrum affected by amplitude attenuation factor.

amplitude attenuation coefficients α will affect the notch depth of the output spectrum. The output of four kinds of amplitude attenuation coefficients is discussed in detail. Values of α are 0.6×10^{-7}, 0.8×10^{-7}, 1.0×10^{-7} and. 1.2×10^{-7}. The corresponding τ were 0.9391, 0.9510, 0.9630, and 0.9274. The channel widens, the resonance peak intensity will gradually decrease, and the band edge tends to be gentle when the loss becomes increasingly large. At this time, values of α and τ are set to 1.0×10^{-7} and 0.9630.

4.4. Quality factor *Q*

The quality factor is used to measure the storage energy of the resonant cavity, which is the ratio of stored energy to dissipation energy. The quality factor is the ratio of peak wavelength to peak half-width expressed as follows:

$$Q = \frac{\lambda}{\mathrm{FWHM}} \tag{14}$$

The embedded microring resonator presents a high Q factor under the condition that other parameters are optimized. The relationship between the self-coupling coefficient and the Q factor is illustrated in Fig. 12. The quality factor of the resonant structure increases with the increase of the radius. The increase of the self-coupling coefficient also increases the slope of the Q factor curve. However, the radius of the U-shaped feedback waveguide will increase, the loss will also increase, and the output strength will change accordingly when the radius of the microring in the proposed structure is increased. The ideal condition should be selected according to the situation. A large radius should be selected to realize the optimal result of the Q factor when the self-coupling coefficient and attenuation factor have been determined.

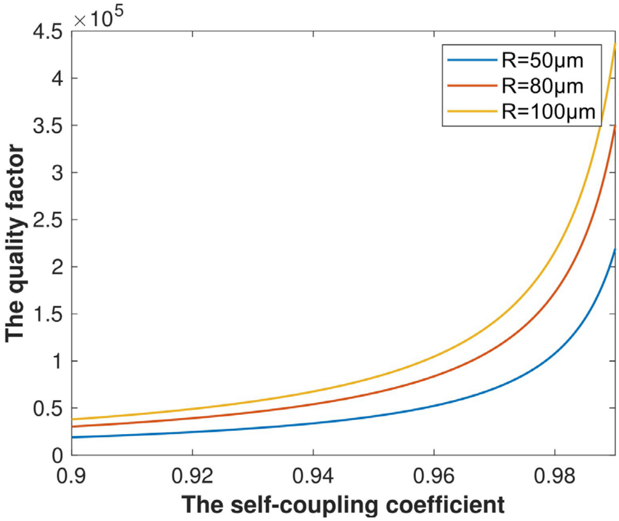

Fig. 12. Relationship between self-coupling factor and quality factor under different microring radius.

4.5. Model sensitivity and detection limit analysis

COMSOL Multiphysics is used to simulate the relevant parameters of the resonator many times, to determine the optimized parameters. The loss coefficient $\alpha = 1\times10^{-7}$, the self-coupling coefficient $t = 0.9849$, and the radius of the ring resonator $R = 100$ μm. Figure 13 shows the output light intensity spectrum of the optimized structure. The resonant wavelength output of the embedded microring resonator is large, and the resonant peak is sharp. The effective refractive index change $\Delta n \approx 4.8\times10^{-5}$, the normalized output light intensity change $\Delta I_0 \approx 0.8671$, the calculation shows that the sensing sensitivity of the structure is 1806.61 dB/RIU, and the extinction ratio is 55.9560 dB. The corresponding detection limit is 1.66056×10^{-7} dB/RIU in the measurement system with a signal-to-noise ratio of 30 dB.

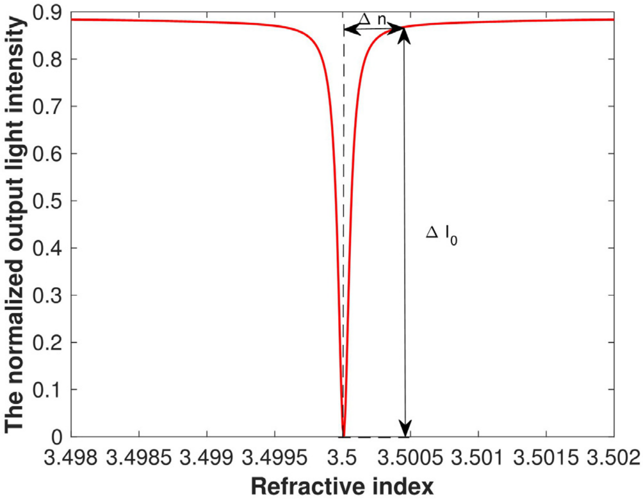

Fig. 13. The relationship between the optimized refractive index and the output light intensity.

5. Conclusions

An embedded microring resonator with PtS_2 material as the core layer and SiO_2 and Si_3N_4 as the cladding was proposed in this study. The device demonstrated robust optical localization and high quality when a high refractive index material layer was introduced. COMSOL Multiphysics was used to investigate the field strength distribution of the longitudinal section of the microring at a resonant wavelength of 1.55086 μm. Parameters, such as self-coupling and loss coefficients affecting spectral output characteristics, were analyzed. The results showed that the free spectral range can be doubled when the radius of the microring is 100 μm, and the length of the U-shaped feedback waveguide L_1 is equal to the perimeter L of the microring. The structural sensitivity is 1806.61 dB/RIU, and the Q factor is 2.8848×10^5. The detection limit is about 1.66056×10^{-7} dB/RIU, and the extinction ratio is 55.9560 dB in the measurement system with a signal-to-noise ratio of 30 dB, thereby indicating satisfactory sensing characteristics. The findings reported in this study provides new insights into the application of graphene-like materials in the optical field and a reference for the fabrication of high-sensing characteristic microring sensors with an extensive measurement range and low detection limit based on two-dimensional materials.

Acknowledgements

This work was supported in part by Science and Technology Program of Hebei under Grant 206Z1703G, in part by Science and Technology Project of Hebei Education Department under Grant ZD2022087, in part by Fundamental Research Funds for Provincial Universities under Grant 2021JK03

References

[1] Bao W., Cai X., Kim D., Sridhara K., Fuhrer M.S., *High mobility ambipolar MoS_2 field-effect transistors: Substrate and dielectric effects*, Applied Physics Letters **102**(4), 2013: 042104. https://doi.org/10.1063/1.4789365

[2] Rohaizad N., Mayorga-Martinez C.C., Sofer Z., Webster R.D., Pumera M., *Layered platinum dichalcogenides (PtS_2, $PtSe_2$, $PtTe_2$) for non-enzymatic electrochemical sensor*, Applied Materials Today **19**, 2020: 100606. https://doi.org/10.1016/j.apmt.2020.100606

[3] Guo G.Y., Liang W.Y., *The electronic structures of platinum dichalcogenides: PtS_2, $PtSe_2$ and $PtTe_2$*, Journal of Physics C: Solid State Physics **19**(7), 1986: 995-1008. https://doi.org/10.1088/0022-3719/19/7/011

[4] Sajjad M., Montes E., Singh N., Schwingenschlögl U., *Superior gas sensing properties of monolayer $PtSe_2$*, Advanced Materials Interfaces **4**(5), 2017: 1600911. https://doi.org/10.1002/admi.201600911

[5] Zhao Y., Qiao J., Yu Z., Yu P., Xu K., Lau S.P., Zhou W., Liu Z., Wang X., Ji W., Chai Y., *High-electron-mobility and air-stable 2D layered $PtSe_2$ FETs*, Advanced Materials **29**(5), 2017: 1604230. https://doi.org/10.1002/adma.201604230

[6] Yuan J., Mu H., Li L., Chen Y., Yu W., Zhang K., Sun B., Lin S., Li S., Bao Q., *Few-layer platinum diselenide as a new saturable absorber for ultrafast fiber lasers*, ACS Applied Materials and Interfaces **10**(25), 2018: 21534-21540. https://doi.org/10.1021/acsami.8b03045

[7] Ermolaev G., Voronin K., Baranov D.G., Kravets V., Tselikov G., Stebunov Y., Yakubovsky D., Novikov S., Vyshnevyy A., Mazitov A., Kruglov I., Zhukov S., Romanov R., Markeev A.M., Arsenin A., Novoselov K.S., Grigorenko A.N., Volkov V., *Topological phase singularities in atomically thin high-refractive-index materials*, Nature Communications **13**, 2022: 2049. https://doi.org/10.1038/s41467-022-29716-4

[8] Li T., Dong H., Hao Y., Zhang Y., Chen S., Xu M., Zhou Y., *Near-infrared responsive photoelectrochemical biosensors*, Electroanalysis **34**(6), 2021: 956-965. https://doi.org/10.1002/elan.202100355

[9] Yim C., Lee K., McEvoy N., O'Brien M., Riazimehr S., Berner N.C., Cullen C.P., Kotakoski J., Meyer J.C., Lemme M.C., Duesberg G.S., *High-performance hybrid electronic devices from layered $PtSe_2$ films grown at low temperature*, ACS Nano **10**(10), 2016: 9550-9558. https://doi.org/10.1021/acsnano.6b04898

[10] Antonacci G., Elsayad K., Polli D., *On-chip notch filter on a silicon nitride ring resonator for Brillouin spectroscopy*, ACS Photonics **9**(3), 2022: 772-777. https://doi.org/10.1021/acsphotonics.2c00005

[11] Yang F., Zhang W., Jiang Y., Tao J., He Z., *Highly sensitive integrated photonic sensor and interrogator using cascaded silicon microring resonators*, Journal of Lightwave Technology **40**(9), 2022: 3055-3061. https://doi.org/10.1109/JLT.2022.3145501

[12] Dehghani F., Abdollahi M., Mohammadi S., Barekatain B., *HDMS: high-performance dual-shaped microring-resonator-based optical switch*, Optical Engineering **61**(3), 2022: 035105. https://doi.org/10.1117/1.OE.61.3.035105

[13] Jin M., Wei Z., Meng Y., Shu H., Tao Y., Bai B., Wang X., *Silicon-based graphene electro-optical modulators*, Photonics **9**(2), 2022: 82. https://doi.org/10.3390/photonics9020082

[14] Cai D.-P., Lu J.-H., Chen C.-C., Lee C.-C., Lin C.-E., Yen T.-J., *High Q-factor microring resonator wrapped by the curved waveguide*, Scientific Reports **5**, 2015: 10078. https://doi.org/10.1038/srep10078

[15] Marsh O.A., Xiong Y., Ye W.N., *Slot waveguide ring-assisted Mach–Zehnder interferometer for sensing applications*, IEEE Journal of Selected Topics in Quantum Electronics **23**(2), 2017: 440-443. https://doi.org/10.1109/JSTQE.2016.2617084

[16] Wan S., Niu R., Ren H.-L., Zou C.-L., Guo G.-C., Dong C.-H., *Experimental demonstration of dissipative sensing in a self-interference microring resonator*, Photonics Research **6**(7), 2018: 681 -685. https://doi.org/10.1364/PRJ.6.000681

[17] Amiri I.S., Rashed A.N.Z., *Power enhancement of the U-shape cavity microring resonator through gap and material characterizations*, Journal of Optical Communications, 2019. https://doi.org/10.1515/joc-2019-0108

[18] Li Z., Bai L., Li X., Gu E., Niu L., Zhang X., *U-shaped micro-ring graphene electro-optic modulator*, Optics Communications **428**, 2018: 200-205. https://doi.org/10.1016/j.optcom.2018.07.062

[19] Campa A., Consolino L., Ravaro M., Mazzotti D., Vitiello M.S., Bartalini S., De Natale P., *High-Q resonant cavities for terahertz quantum cascade lasers*, Optics Express **23**(3), 2015: 3751 -3761. https://doi.org/10.1364/OE.23.003751

[20] Ermolaev G.A., Voronin K.V., Tatmyshevskiy M.K., Mazitov A.B., Slavich A.S., Yakubovsky D.I., Tselin A.P., Mironov M.S., Romanov R.I., Markeev A.M., Kruglov I.A., Novikov S.M., Vyshnevyy A.A., Arsenin A.V., Volkov V.S., *Broadband optical properties of atomically thin* PtS_2 *and* $PtSe_2$, Nanomaterials **11**(11), 2021: 3269. https://doi.org/10.3390/nano11123269

Received June 3, 2022
in revised form August 2, 2022